Nanotechnology

Revealing misfit dislocations in InAs$_x$P$_{1-x}$-InP core–shell nanowires by x-ray diffraction

View the article online for updates and enhancements.

Revealing misfit dislocations in InAs$_x$P$_{1-x}$-InP core–shell nanowires by x-ray diffraction

Sergey Lazarev[1,2] , David J O Göransson[3], Magnus Borgström[3] ,
Maria E Messing[3] , H Q Xu[3,4] , Dmitry Dzhigaev[1,11] ,
Oleksandr M Yefanov[5], Sondes Bauer[6], Tilo Baumbach[6,7],
Robert Feidenhans'l[8,9], Lars Samuelson[3] and Ivan A Vartanyants[1,10]

[1] Deutsches Elektronen-Synchrotron DESY, Notkestraße 85, D-22607 Hamburg, Germany
[2] National Research Tomsk Polytechnic University (TPU), pr. Lenina 30, 634050 Tomsk, Russia
[3] NanoLund, Division of Solid State Physics, Lund University, Box 118, S-22100 Lund, Sweden
[4] Beijing Key Laboratory of Quantum Devices, Key Laboratory for the Physics and Chemistry of Nanodevices, and Department of Electronics, Peking University, Beijing 100871, People's Republic of China
[5] Center for Free-Electron Laser Science, DESY, Notkestraße 85, D-22607 Hamburg, Germany
[6] Institute for Photon Science and Synchrotron Radiation IPS, Karlsruhe Institute of Technology KIT, Hermann-vonHelmholtz-Platz 1, D-76344 Eggenstein-Leopoldshafen, Germany
[7] Laboratory for Application of Synchrotron Radiation LAS, Karlsruhe Institute of Technology, Kaiserstraße12, D-76131 Karlsruhe, Germany
[8] Niels Bohr Institute, University of Copenhagen, Universitetsparken 5, DK-2100 Copenhagen, Denmark
[9] European XFEL GmbH, Holzkoppel 4, D-22869 Schenefeld, Germany
[10] National Research Nuclear University MEPhI (Moscow Engineering Physics Institute), Kashirskoe shosse 31, 115409 Moscow, Russia

E-mail: dr.s.lazarev@gmail.com

CrossMark

Abstract

InAs$_x$P$_{1-x}$ nanowires are promising building blocks for future optoelectronic devices and nanoelectronics. Their structure may vary from nanowire to nanowire, which may influence their average optoelectronic properties. Therefore, it is highly important for their applications to know the average properties of an ensemble of the nanowires. Structural properties of the InAs$_x$P$_{1-x}$-InP core–shell nanowires were investigated using the coplanar x-ray diffraction performed at a synchrotron facility. Studies of series of symmetric and asymmetric x-ray Bragg reflections allowed us to determine the 26% ± 3% of As chemical composition in the InAs$_x$P$_{1-x}$ core, core–shell relaxation, and the average tilt of the nanowires with respect to the substrate normal. Based on the x-ray diffraction, scanning, and transmission electron microscopy measurements, a model of the core–shell relaxation was proposed. Partial relaxation of the core was attributed to misfit dislocations formed at the core–shell interface and their linear density was estimated to be $3.3 \pm 0.3 \times 10^4$ cm^{-1}.

Supplementary material for this article is available online

---

[11] Current address: Division of Synchrotron Radiation Research, Department of Physics, Lund University, Box 118, S-22100, Lund, Sweden.

Introduction

The $A_{III}B_V$ semiconductor nanowires (NWs) are one-dimensional nanostructures based on such materials as indium phosphide (InP), indium arsenide (InAs), and indium arsenide phosphide ($InAs_xP_{1-x}$). They have attracted increasing attention due to their unique properties related to surface and quantum confinement effects allowing application for transistors, solar cells, single photon sources, lasing, sensors, qubits or thermoelectric materials, and light-emitting diodes [1–3].

There are still many challenges to grow NWs, to design p–n junctions, to control the composition and structure of their alloys ($InAs_xP_{1-x}$), and to manufacture metallic contacts to them. As an additional difficulty, the typical structure for the $InAs_xP_{1-x}$ NWs is a mixture of zinc-blende (ZB) and wurtzite (WZ) phases called polymorphism [3, 4]. In the present work, we do not discuss polymorphism of the NWs, which was investigated elsewhere [5, 6]. Here, we assume, based on the electron microscopy and x-ray diffraction studies, that the structure of the NWs is pure wurtzite.

Semiconductor NWs are commonly studied using different experimental techniques such as transmission electron microscopy (TEM), scanning electron microscopy (SEM), cathodoluminescence (CL), etc [3, 7, 8]. Most of these methods are usually local, require destructive sample preparation or could provide information only about the surface of the NWs. In the present work, a non-destructive x-ray diffraction method was used to study $InAs_xP_{1-x}$-InP core–shell NWs. The x-ray diffraction on NWs can be performed to study crystallographic properties of a single nanostructure by the x-ray beam focused down to few micrometers or even to nanometer scale [9–12]. In this case, information is obtained only for one object of the ensemble of nanostructures. Therefore, an additional investigation of averaged properties may be needed [5, 13]. For this purpose, large x-ray beams of about hundreds of microns may be useful to study many illuminated semiconductor NWs.

This research aimed to investigate the structure of an ensemble of $InAs_xP_{1-x}$-InP core–shell NWs grown on (111) InP substrate using a combination of coplanar x-ray diffraction, SEM, and TEM measurements.

Experiment

Sample

The $InAs_xP_{1-x}$-InP core–shell NWs were grown in [0001] direction on (111)B InP ZB substrate in a low-pressure (100 mbar) metal-organic vapor phase epitaxy reactor at the center for nanoscience 'NanoLund' at Lund University. The growth of the core of the NWs was performed with the gold (Au) seed particles with a diameter of 40 nm that were deposited in an aerosol particle generator [14].

During the growth of the $InAs_xP_{1-x}$ WZ cores, following the methods in [15] the reactor temperature was set to 420 °C and the growth precursors used were phosphine (PH_3) with a molar fraction $\chi_{PH_3} = 6.2 \times 10^{-3}$, trimethylindium (TMIn) with a molar fraction $\chi_{TMIn} = 7.1 \times 10^{-6}$ and arsine (AsH_3) with a molar fraction $\chi_{AsH_3} = 2.75 \times 10^{-5}$. These molar fractions were fixed to define a content x of InAs in the range of 24%–28%. Additionally hydrogen chloride (HCl) with a molar fraction $\chi_{HCl} = 2.3 \times 10^{-5}$ was used to control radial growth [16] and hydrogen sulfide (H_2S) was used as n-type dopant. The core of the NWs was grown in three steps having different hydrogen sulfide precursor molar fractions χ_{H_2S}. This was done in order to achieve high n-type doping in the ends of the nanowire and low doping in the center, to enable fabrication of ohmic contacts for studies of the optoelectronic properties of the NWs. The dopant molar fraction χ_{H_2S} was initially 7.1×10^{-7}, after 4 min growth the χ_{H_2S} was decreased for 3 min to a 1.1×10^{-7} for lower doping content. Finally, the growth continued for 8 min with χ_{H_2S} changed back to the value 7.1×10^{-7}.

Next, the InP WZ shell of the NWs was grown at 550 °C for 8 min, using only the source gases TMIn and PH_3, with molar fractions $\chi_{PH_3} = 3.7 \times 10^{-2}$ and $\chi_{TMIn} = 4.0 \times 10^{-6}$, respectively. The InP WZ shell is expected to grow epitaxially on the $InAs_xP_{1-x}$ WZ core. Schematic structure of a core–shell NW is shown in figure 1(a). Two $InAs_xP_{1-x}$ segments of the NW's core with the sulfur dopant content are marked as n_1 and n_2. In the manuscript, we will use a Cartesian coordinate system xyz with the z-axis perpendicular to the surface of the substrate depicted in figure 1(a).

SEM measurements

The NWs were first investigated by the SEM measurements with an accelerating voltage of 10 kV at Lund University. Initially, the sample with only the $InAs_xP_{1-x}$ cores was studied. Its SEM image is presented in figure 1(b). The diameter of the cores was measured to be about 45 nm and the total length of about 4.5 μm. The average density of the NWs was estimated from the seed particles density and the SEM measurements to be about 0.4 μm^{-2}.

Further, the sample with the $InAs_xP_{1-x}$-InP core–shell NWs was measured (see the SEM image in figure 1(c) and an enlarged image in figure 1(d)). The total diameter of the NWs in our experiment was measured to be 95 $\pm$ 3 nm. Therefore, the resulting shell thickness of the NWs is 25 $\pm$ 2 nm.

As one can see from figure 1(c), additional parasitic growth of InP droplet on the top of NWs has happened. The grown InP material has ZB structure, which was confirmed by TEM measurements (see the supporting information available
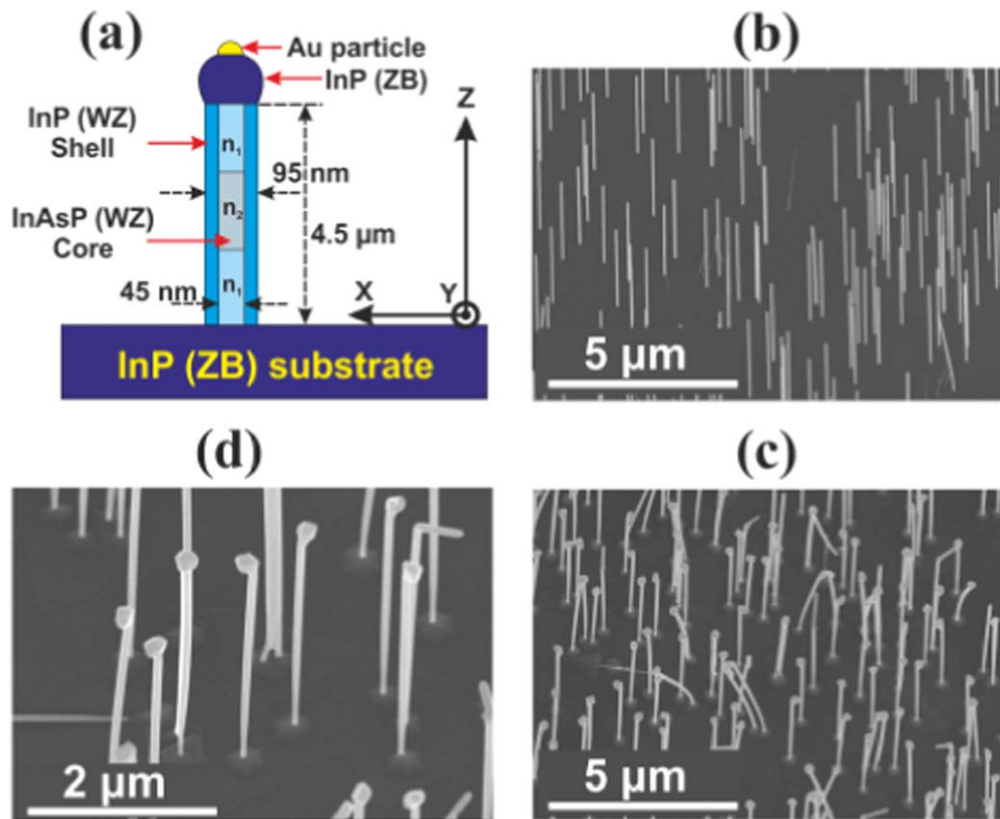
Figure 1. (a) Schematic presentation of an InAs$_x$P$_{1-x}$-InP core–shell nanowire structure with a Cartesian coordinate system. Two parts of the NW have the same dopant H$_2$S content marked as n_1. The central part of the NWs, which has seven times lower H$_2$S content marked as n_2. The SEM images of the sample surface after growth of the InAs$_x$P$_{1-x}$ WZ core (b) and InAs$_x$P$_{1-x}$-InP WZ core–shell nanowires (c). (d) An enlarged SEM image of the InAs$_x$P$_{1-x}$-InP core–shell nanowires. All SEM images are measured at a tilt angle of the sample surface of 30°.
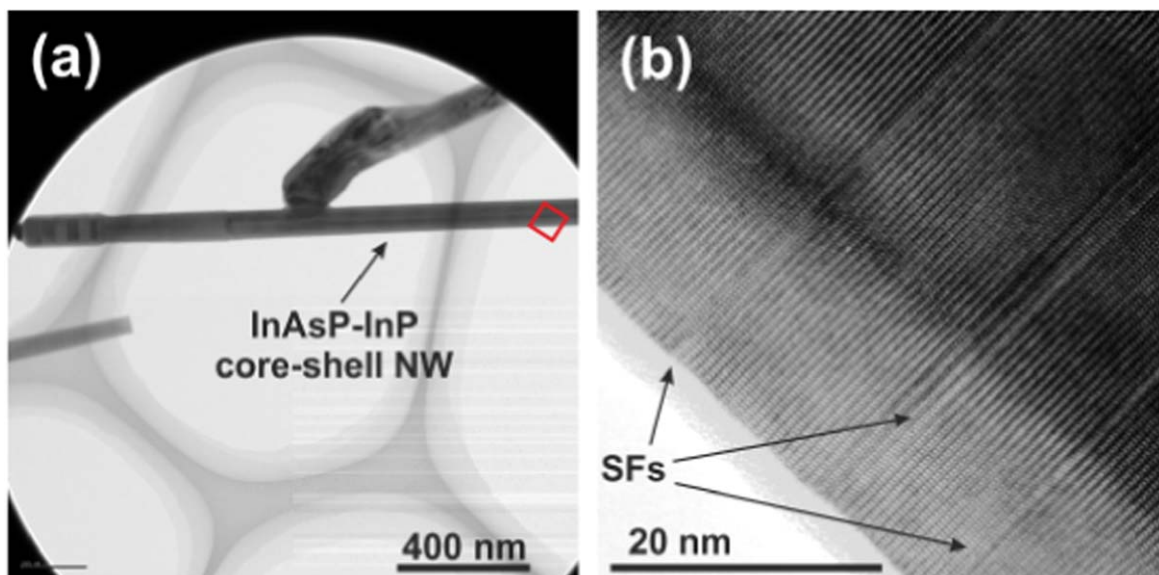
Figure 2. TEM measurements of an InAs$_{0.26}$P$_{0.74}$-InP WZ core–shell NW. (a) High-angle annular dark-field (HAADF) TEM image with a general view of a NW under investigation. (b) High-resolution TEM image of a part of the NW with atomic resolution. (a) The investigated part of the NW is shown as a red square. The HRTEM image demonstrates presence of stacking faults in the InP shell, which are marked as stacking faults.

online at stacks.iop.org/NANO/30/505703/mmedia). Comparison of figures 1(b) and (c) demonstrates a tilt of the core–shell NWs with respect to the substrate, which was already observed in previous works [12, 17]. In our study, this bending of the NWs is more probably due to the random geometry of the ZB droplets on top of the NWs.

TEM measurements

The TEM measurements of the NWs were performed at the national center for high-resolution electron microscopy (nCHREM) on a JEOL 3000F TEM equipped with a field emission gun and operated at 300 kV. The high-angle annular dark-field TEM image with a general view of an InAs$_{0.26}$P$_{0.74}$-InP WZ core–shell NW under investigation is shown in figure 2(a). This scan covers a relatively large area of the NW, but with a low resolution.

To resolve a local structure of the NW, the high-resolution TEM (HRTEM) imaging was performed on several parts of the NW and an area with an atomic resolution is presented in figure 2(b). The HRTEM image demonstrates the presence of stacking faults in the InP shell, which are depicted in figure 2(b). These stacking faults correspond to polymorphism in the NWs and are a mixture of ZB and WZ phases [3, 4]. However, the number of ZB layers is minimal, and the NWs are, therefore, assumed to be pure WZ in our study. Furthermore, the stacking faults do not contribute significantly to the x-ray diffraction due to their low density. Presence of the stacking faults in the shell allows expecting that some of them are formed due to the misfit dislocations (MDs) located between the core and the shell of the NWs.

Coplanar x-ray diffraction

Laboratory x-ray diffraction

First, an x-ray diffraction study of the sample with the wavelength of 1.541 Å (energy of 8.046 keV) were performed at a laboratory x-ray source at NanoLund, Lund University, Sweden. The scheme of the experiment is shown in figure 3(a). From the structure of the InAs$_x$P$_{1-x}$ core NWs and the InP substrate, two Bragg reflections in reciprocal space were expected, namely, 111 InP and 0002 InAs$_x$P$_{1-x}$ Bragg peaks. Here and further we will use three indices notation for ZB and four for WZ structures. An expected reciprocal space map (RSM) of the sample is schematically shown in figure 3(b).

The sample with only InAs$_x$P$_{1-x}$ cores was studied at the laboratory x-ray source by employing $2\Theta - \omega$ scan through the maximum of 111 InP Bragg peak. This scan in reciprocal space is marked as 'A' in figure 3(b) and is parallel to the Q_z-axis of the corresponding Cartesian coordinate system (see figure 3(b)). The intensity distribution of this scan is presented in figure 3(c) (black curve) and demonstrates presence of the expected diffraction signals. Due to the dominant contribution of the InP substrate signal, intensity of the InAs$_x$P$_{1-x}$ NWs Bragg peak is suppressed. In order to enhance this signal, the second $2\Theta - \omega$ scan 'B' was performed at an offset angle $\gamma = 0.2°$ with respect to the scan 'A', which corresponds to a shift in reciprocal space along Q_x by $\delta Q_x = 0.07$ nm^{-1} (see figure 3(b)). The intensity distribution of the scan 'B' is presented in figure 3(c) (brown curve) and demonstrates a symmetric shape of the 0002 InAs$_x$P$_{1-x}$ Bragg peak. From the $Q_z = 18.32$ nm^{-1} coordinate of the Bragg peak composition x of InAs in InAs$_x$P$_{1-x}$ alloy can

be determined. The unit cell lattice parameters of the WZ InP and InAs NWs are known to be $a_{InP} = 4.14$ Å and $c_{InP} = 6.80$ Å for the WZ InP [18], and $a_{InAs} = 4.27$ Å and $c_{InAs} = 7.03$ Å for WZ InAs [19]. The InAs$_x$P$_{1-x}$ unit cell lattice parameter c_{InAsP} obtained from the Q_z peak position is 6.86 Å. Since the NWs with only InAs$_x$P$_{1-x}$ core are fully relaxed, the composition x of InAs according to the Vegard's law for the ternary alloys [20–22] could be calculated as

$$x = \frac{c_{InAsP} - c_{InP}}{c_{InAs} - c_{InP}} = 0.26 \pm 0.03, \tag{1}$$

and the unit cell lattice parameters of the relaxed WZ InAs$_{0.26}$P$_{0.74}$ core are $a_{InAsP} = 4.18 \pm 0.03$ Å and $c_{InAsP} = 6.86 \pm 0.04$ Å.

Further, the sample with InAs$_{0.26}$P$_{0.74}$-InP core–shell NWs was investigated using the same experimental scheme (see figures 3(b) and (c)). Theoretical lattice mismatch between the InP shell and the InAs$_{0.26}$P$_{0.74}$ core is

$$M_0 = \frac{c_{InP} - c_{InAsP}}{c_{InAsP}} = -8.7 \pm 0.6 \times 10^{-3}. \tag{2}$$

Taking into account the core–shell relaxation [23], similar Bragg peak at a different position in RS was predicted for the InAs$_{0.26}$P$_{0.74}$-InP core–shell NWs. Unexpectedly, the WZ core–shell NWs 0002 Bragg peak in $2\Theta - \omega$ scan 'B' revealed double maxima structure marked as '1' and '2' in figure 3(c) (magenta curve). Positions of the peaks were obtained by a fit of the x-ray diffraction curve with three Gaussian functions shown in figure 3(d). Parameters of the Gaussian functions are Peak(1): $Q_z = 18.41 \pm 0.06$ nm^{-1}, Peak(2): $Q_z = 18.39 \pm 0.08$ nm^{-1}. These Q_z coordinates correspond to the unit cell lattice parameters $c_{Peak(1)} = 6.82 \pm 0.05$ Å, $c_{Peak(2)} = 6.84 \pm 0.08$ Å. The intensity of the Peak(1) is approximately two times higher than the intensity of the Peak(2) taking into account the ratio of the area below Gaussian distributions from the fit. In order to understand the origin of the NWs Bragg peak double structure, x-ray diffraction measurements at a synchrotron source were performed.

Experimental setup at a synchrotron

The synchrotron x-ray diffraction measurements were performed at a bending magnet single-crystal diffraction beamline at the synchrotron facility ANKA in Karlsruhe, Germany. The RSMs of the sample were recorded with a monochromatic x-ray beam at an energy of 12 keV. Measurements were performed at a six circle diffractometer with four degrees of freedom for the sample and two degrees of freedom for the detector. The x-ray beam was focused to the center of the diffractometer down to the size of about 500×500 μm^2. All x-ray data were recorded with a microstrip solid-state linear detector Mythen 1K. The detector has a total number of 1280 channels with a channel size of 50 μm $\times$ 8 mm and a point-spread function of one channel. The sample to detector distance in the experiment was about 0.7 m, which corresponds to an angular resolution of about 0.004° per pixel [24, 25]. The sample was measured in a coplanar x-ray diffraction geometry with the surface normal, an incidence and diffracted x-ray beams lying in the same diffraction plane [26].
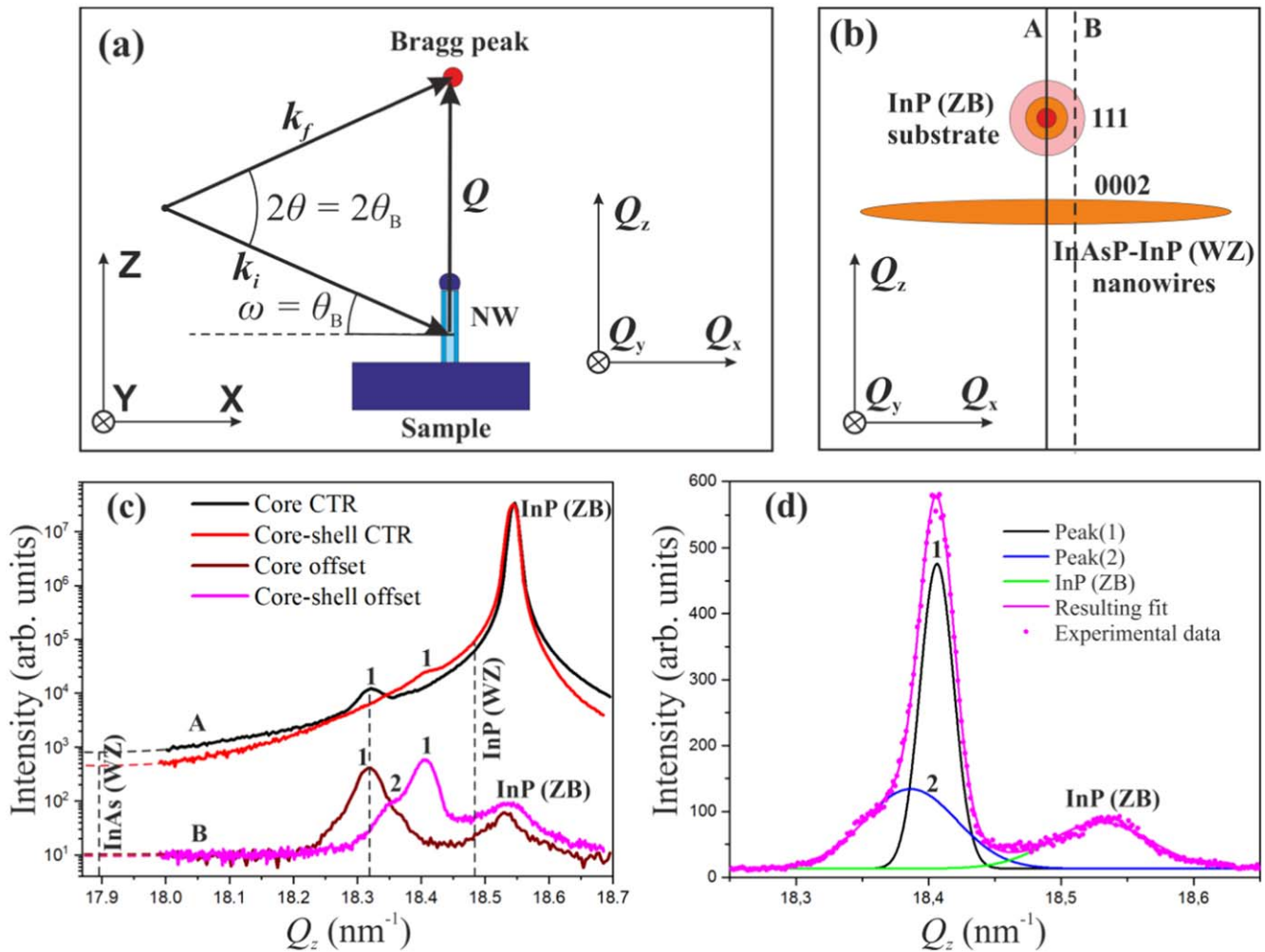
Figure 3. (a) Scheme of the laboratory x-ray diffraction experiment. The incident $\mathbf{k}_i$ and the outgoing $\mathbf{k}_f$ x-ray wave vectors define the scattering vector $\mathbf{Q} = \mathbf{k}_f - \mathbf{k}_i$. Cartesian coordinate system $Q_x Q_y Q_z$ in reciprocal space has axis parallel to the *xyz* axis of the coordinate system in real space (see figure 1(a)). In the scheme, ω is the incident angle and 2Θ is the angle between vectors $\mathbf{k}_f$ and $\mathbf{k}_i$. (b) Reciprocal space scheme of the 0002 InAs$_x$P$_{1-x}$-InP core–shell NWs and 111 InP substrate Bragg reflections. The sample was scanned by $2\Theta - \omega$ scans through the maximum of 111 InP Bragg peak marked as 'A' and along a direction 'B' inclined by an angle $\gamma = 0.2°$ with respect to the scan 'A', which corresponds to a shift in reciprocal space along Q_x by $\delta Q_x = 0.065$ nm^{-1}. (c) The intensity distributions of the scans 'A' and 'B' of the samples with only InAs$_x$P$_{1-x}$ WZ cores and InAs$_x$P$_{1-x}$-InP WZ core–shell NWs. (d) Fit of the Bragg peaks 1, 2 of the InAs$_x$P$_{1-x}$-InP core–shell NWs and InP with three Gaussian functions.

Symmetric x-ray diffraction (SXRD) at a synchrotron

At the synchrotron source a series of full SXRD RSMs of 111/0002, 222/0004, 333/0006, and 444/0008 Bragg reflections were measured and are presented in figure 4(a). Taking into account the x-ray beam size and its incidence angle for these reflections, the average number of illuminated InAs$_{0.26}$P$_{0.74}$ NWs was estimated to be about 10^5. In the RSMs (see figure 4(a)), several maxima of diffraction intensity are visible. The most intense diffraction signal originating from the InP substrate is marked as InP in figure 4(a). Two broad Bragg peaks along Q_x direction are attributed to the signals from the InAs$_{0.26}$P$_{0.74}$-InP core–shell NWs. The intensity streak along Q_x direction in the vicinity of the InP Bragg peak well pronounced in the reflection 111 (see figure 4(a)) is attributed to the signal from the parasitically grown InP droplets on the top of NWs (see figure 1(d)). This

signal is invisible in other reflections due to the lower intensity value in comparison to the substrate scattering. Additionally, two streaks of intensities crossing the InP Bragg peak are present in the RSMs in figure 4(a). The vertical one that goes parallel to the Q_z-axis through the origin of reciprocal space is a crystal truncation rod (CTR) [24, 27]. The CTR is absent in the RSM of the reflection 444 due to a low intensity of the reflection and a possible small misalignment of the sample surface. The second streak is inclined to the CTR at the Bragg angle of the corresponding reflection. This streak corresponds to a detector frame (position of the Ewalds sphere) with increased background due to the x-rays scattering on air. The parasitic background is a result of the raised x-ray scattering intensity from the substrate in the exact Bragg conditions and is called a detector streak (D) [24].

Experimentally measured distribution of intensity in reciprocal space along the CTR for all reflections is presented
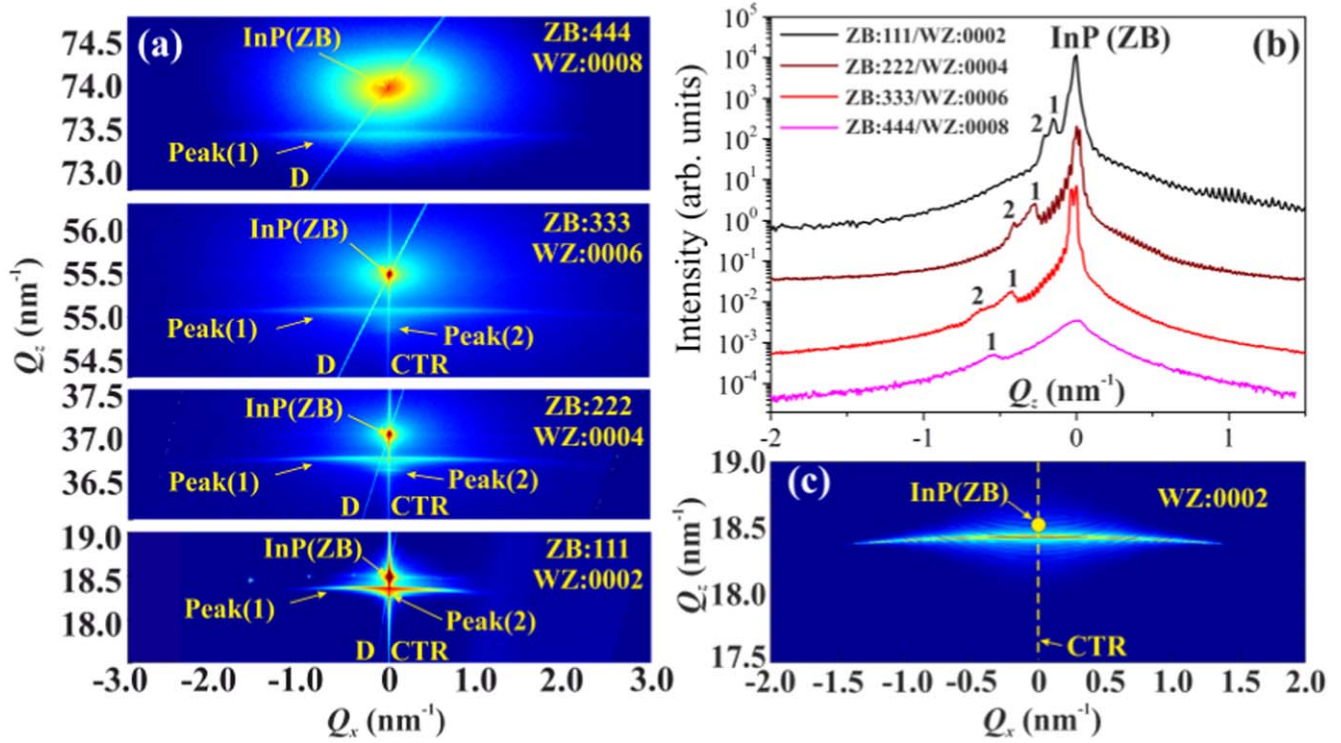
Figure 4. (a) Reciprocal space maps of the symmetric ZB/WZ 111/0002, 222/0004, 333/0006, and 444/0008 Bragg reflections in logarithmic scale. (b) Their intensity distributions along the CTR. For better representation each plot of the intensity distribution in (b) was shifted by one order of magnitude. Numbers '1' and '2' depict positions of the Bragg reflections Peak(1) and Peak(2). (c) Monte Carlo simulation results of the 0002 Bragg peak of the InAs$_{0.26}$P$_{0.74}$-InP core–shell NWs based on a NW model with the shell thickness variation (see for details the supporting information). Position of the 111 InP Bragg peak and the CTR are also shown in RSM.

Table 1. The Q_z values of symmetric reflections and the unit cell lattice parameters c obtained from the Bragg peaks ZB InP, WZ Peak(1), Peak(2), and the FEM model.

	$Q_z^{111/0002}$ (nm^{-1})	$Q_z^{222/0004}$ (nm^{-1})	$Q_z^{333/0006}$ (nm^{-1})	$Q_z^{444/0008}$ (nm^{-1})	c (Å)
InP(ZB)	18.54 ± 0.01	37.08 ± 0.01	55.62 ± 0.01	74.16 ± 0.02	6.78 ± 0.01
Peak(1)	18.33 ± 0.01	36.71 ± 0.01	55.07 ± 0.02	73.44 ± 0.03	6.83 ± 0.02
Peak(2)	18.27 ± 0.02	36.57 ± 0.02	54.86 ± 0.03	—	6.86 ± 0.03
Peak(FEM)	18.44 ± 0.01	36.88 ± 0.01	55.32 ± 0.01	73.76 ± 0.01	6.82 ± 0.01

in figure 4(b). The intensity distribution reveals the presence of two Bragg diffraction signals originating from the InAs$_{0.26}$P$_{0.74}$-InP core–shell NWs. The Q_z coordinates of the Bragg peaks for all measured symmetric reflections and corresponding unit cell lattice parameters c are summarized in table 1. From the parameters of $c_{\text{Peak(1)}}$ and $c_{\text{Peak(2)}}$, the experimental lattice misfits between the relaxed InAs$_{0.26}$P$_{0.74}$ core and the detected lattice parameters of the NWs can be calculated as

$$M_1^c = \frac{c_{\text{Peak(1)}} - c_{\text{InAsP}}}{c_{\text{InAsP}}} = -4.2 \pm 0.4 \times 10^{-3},$$

$$M_2^c = \frac{c_{\text{Peak(2)}} - c_{\text{InAsP}}}{c_{\text{InAsP}}} = -0.7 \pm 0.1 \times 10^{-3}. \quad (3)$$

The parasitic InP ZB layer grown on the InP ZB substrate during the InP WZ shell deposition, which form pyramidal islands in the base of the NWs in figure 1(c), leads to oscillations of the intensity profiles along the CTR in figure 4(b).

From the average period ΔQ_z of 0.03 ± 0.01 nm^{-1}, the corresponding thickness of this layer $\delta = 207 \pm 51$ nm was obtained using equation $\delta = 2\pi/\Delta Q_z$ [26].

Further, the broadening of reflections in Q_x direction was analyzed. The InAs$_{0.26}$P$_{0.74}$ NWs could be considered as tilted and twisted blocks, and a mosaic block model could be applied for the analysis of their symmetric reflections broadening. Therefore, a Williamson–Hall (WH) plot, which is a plot of the full width at half maximum (FWHM) of reflections broadening in an angular Q_x direction as a function of Q_z-coordinate [21, 28], can be used to determine an average tilt of the InAs$_{0.26}$P$_{0.74}$ NWs [3, 24]. From the linear fit of the WH plot, an average value of the NWs angular tilt α and horizontal coherence length L can be obtained [21]

$$\text{FWHM}(Q_z) = tg(\alpha) \cdot Q_z + 2\pi/L. \quad (4)$$

The WH plot was performed for both diffraction peaks Peak(1) and Peak(2) (see figure 4). The intensity distribution along Q_x
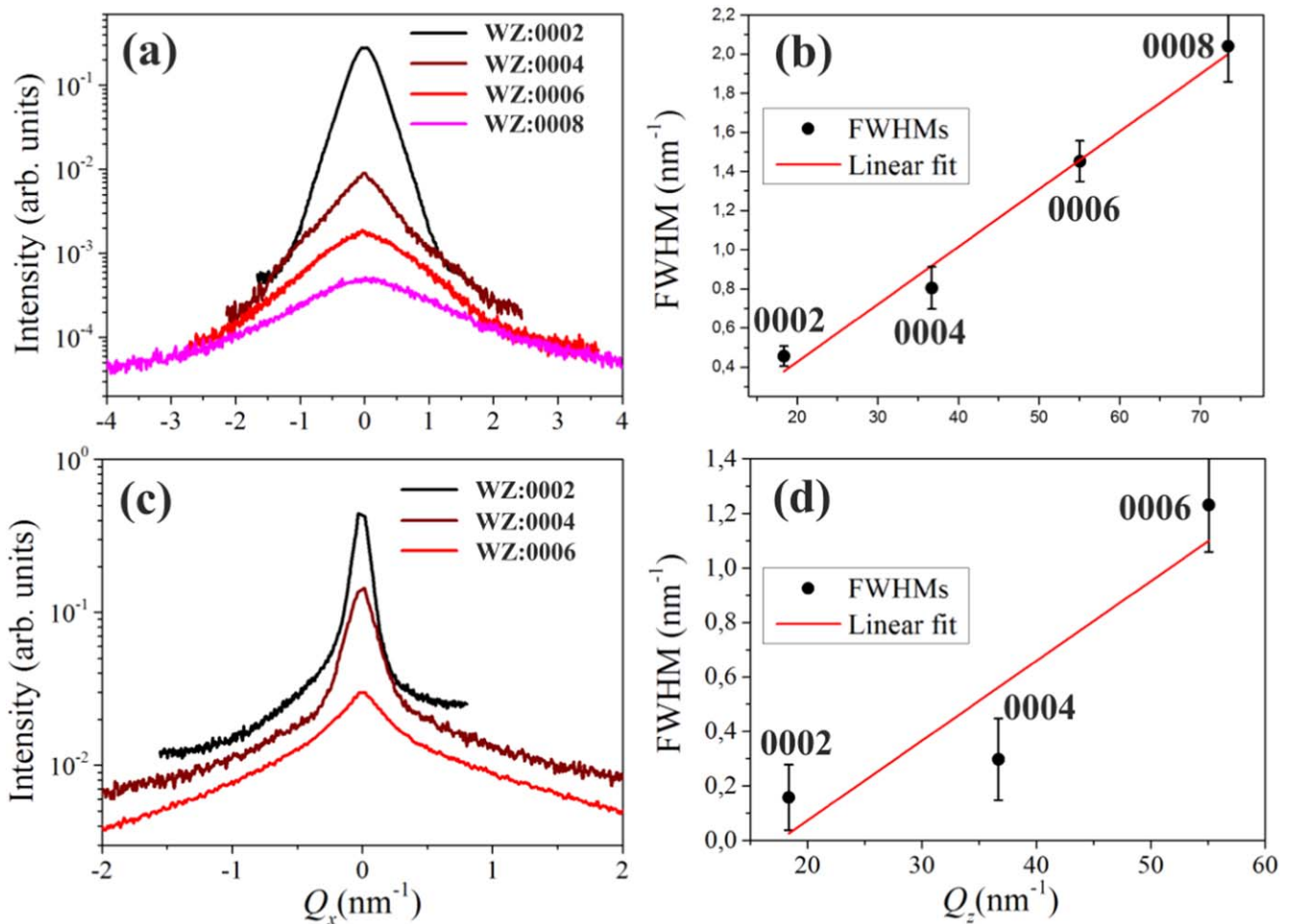
Figure 5. (a) Peak(1) and (c) Peak(2) Bragg peaks intensity distributions of 0002, 0004, 0006, and 0008 reflections along the Q_x direction after the subtraction of the crystal truncation rod intensity. Williamson–Hall plots of the Peak(1) (b) and Peak(2) (d) based on the FWHMs of the symmetric reflections.

direction in reciprocal space of all symmetric reflections after the subtraction of the CTR intensity are compared in figures 5(a) and (c). These intensity profiles were fitted with the Gaussian functions and obtained FWHMs were used in the WH plot shown in figures 5(b) and (d). From the WH plots of the symmetric reflections, average slopes of $1.69° \pm 0.14°$ and $1.68° \pm 0.71°$, and intersection value of the linear function with the ordinate -0.016 ± 0.012 nm^{-1} and -0.051 ± 0.049 nm^{-1} were obtained using equation (4). The mean slope of $1.68° \pm 0.71°$ is attributed to the average tilt of the NWs, while the intersection value could not be used for the coherence length calculation due to the high value of the systematic error in our measurements. The slope value is in a good agreement with the experimentally obtained tilt angles of semiconductor nanowires [12, 17, 29].

Asymmetric x-ray diffraction (AXRD) at a synchrotron

Coplanar AXRD RSM of 246 InP substrate and $11\bar{2}8$ InAs$_{0.26}$P$_{0.74}$ NWs reflections was recorded in order to determine the unit cell lattice parameters *a* of the Bragg peaks Peak (1) and Peak(2) from the lateral components $\mathbf{Q}_x$ of their scattering vectors. Schematic comparison of symmetric and asymmetric RSMs shown in figure 6(a) demonstrates different

positions of the Bragg peaks along $\mathbf{Q}_x$ in the case of AXRD. The experimentally measured asymmetric RSM is presented in figure 6(b) (see the supporting information for the initial RSM). In the RSM, the D streak is inclined with respect to the CTR in an angle of about 63°, which equals to the sum of the Bragg angle of the 264 InP reflection (41.20°) and an angle of inclination of the diffraction planes with respect to the sample surface (22.21°). The intensity of the Bragg peaks is lower in comparison to the symmetric diffraction because of the twist of the NWs, which reduces the scattered intensity in the coplanar diffraction plane. Due to relatively high diffuse intensity in the vicinity of the substrate 246 InP Bragg peak, it is difficult to determine precise positions of the WZ Peak(1) and Peak(2) peaks directly. For better representation of the signals Peak(1) and Peak(2), the RSM is shown as a contour plot in figure 6(b). Red lines in the figure outline an elongation of the Peak(1), which is broad due to the tilt of the NWs with respect to the substrate observed in SXRD, and the Peak(2). The fact that these peaks have two components of the diffraction vector $\mathbf{Q}$ in reciprocal space and that Q_z component is already known for both peaks allows precise determination of the second Q_x component. The dashed horizontal lines in figure 6(b) show positions of the Q_z coordinates of the Peak(1) and Peak(2)
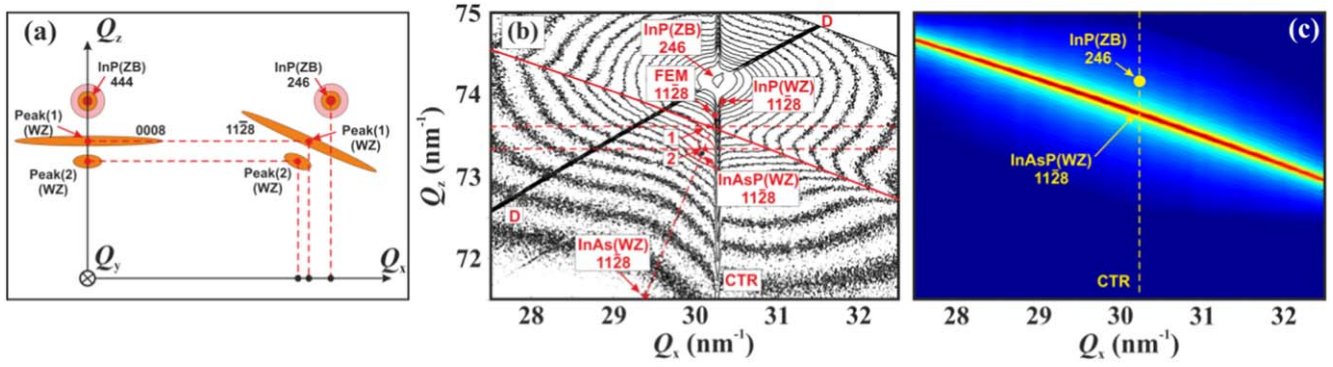
Figure 6. Analysis of the asymmetric coplanar x-ray diffraction map. (a) Scheme of the ZB/WZ 246/11$\bar{2}$8 Bragg reflections AXRD RSM in comparison with the ZB/WZ 444/0008 SXRD RSM. The AXRD measurement reveals the lateral components $\mathbf{Q}_x$ of the scattering vectors. (b) Experimental AXRD RSM is presented as a contour plot (see the supporting information for the initial RSM). The red line in figure (b) outlines an elongation of the Bragg reflection Peak(1), which is due to the tilt of the NWs with respect to the substrate normal, while the red contour lines demonstrate the vicinity of the Bragg reflection Peak(2). The dashed horizontal lines show levels of Q_z components and the red points positions of the Bragg reflections Peak(1) and Peak(2). Numbers '1' and '2' depict the peaks Peak(1) and Peak(2), respectively. Additionally, the 11$\bar{2}$8 Bragg peaks of an InP, InAs, the unstrained InAs$_{0.26}$P$_{0.74}$ core (InAsP(WZ)), and the strained InAs$_{0.26}$P$_{0.74}$-InP core–shell obtained from the FEM model are presented in (b). (c) Monte Carlo simulation results of the AXRD Bragg peak based on the FEM model (see for details the supporting information).

Table 2. Coordinates Q_z, Q_x, and the unit cell lattice parameters a and c of the bulk ZB InP, WZ InP and InAs NWs, FEM model, and the Peak(1) and Peak(2) of ZB/WZ 264/11 $\bar{2}$8 Bragg reflections.

	Q_x (nm^{-1})	Q_z (nm^{-1})	a (Å)	c (Å)
InP(ZB)	30.28 ± 0.02	74.18 ± 0.02	4.15 ± 0.03	6.78 ± 0.01
InP(WZ)	30.34	73.91	4.14	6.80
InAs(WZ)	29.40	71.55	4.27	7.03
Peak(FEM)	30.25 ± 0.01	73.76 ± 0.01	4.15 ± 0.02	6.82 ± 0.01
Peak(1)	30.18 ± 0.02	73.61 ± 0.02	4.16 ± 0.03	6.83 ± 0.02
Peak(2)	30.17 ± 0.05	73.33 ± 0.03	4.17 ± 0.05	6.86 ± 0.03

Bragg peaks. Red points show positions of the Peak(1) and Peak(2) Bragg peaks. From their positions, the unit cell lattice parameter of the peaks Peak(1) and Peak(2) are found to be $a_{\text{Peak}(1)} = 4.16 \pm 0.03$ Å and $a_{\text{Peak}(2)} = 4.17 \pm 0.05$ Å, respectively. Additionally, positions of the 11$\bar{2}$8 Bragg peaks of an InP, InAs, and the unstrained InAs$_{0.26}$P$_{0.74}$ core in reciprocal space are presented in figure 6(b). All coordinates of the Bragg peaks are summarized in table 2.

From the obtained unit cell lattice parameters $a_{\text{Peak}(1)}$ and $a_{\text{Peak}(2)}$, the experimental lattice misfit in [11 $\bar{2}$ 0]-direction between the relaxed InAs$_{0.26}$P$_{0.74}$ core and the detected signal is

$$M_1^a = \frac{a_{\text{Peak}(1)} - a_{\text{InAsP}}}{a_{\text{InAsP}}} = -2.7 \pm 0.4 \times 10^{-3},$$

$$M_2^a = \frac{a_{\text{Peak}(2)} - a_{\text{InAsP}}}{a_{\text{InAsP}}} = -3.0 \pm 0.6 \times 10^{-3}. \quad (5)$$

As one can see from the difference between M_1^a/M_2^a and M_1^c/M_2^c, there is a tetragonal distortion of the structure corresponding to the Bragg peaks (1) and (2), which could be obtained as

$$D_1 = \frac{P_{\text{Peak}(1)} - P_{\text{InAsP}}}{P_{\text{InAsP}}} = -1.5 \pm 0.3 \times 10^{-3},$$

$$D_2 = \frac{P_{\text{Peak}(2)} - P_{\text{InAsP}}}{P_{\text{InAsP}}} = 2.4 \pm 0.5 \times 10^{-3}, \quad (6)$$

where $P = c/a$ is a ratio of the unit cell lattice parameters c and a of the structures. This tetragonal distortion of the structure is due to the strain between the core and the shell, but it is less than the value predicted by the model, which will be presented in the next section.

Model

We have experimentally investigated the InAs$_{0.26}$P$_{0.74}$-InP NWs using different methods. Now, we will model the strain field in the NWs to retrieve the theoretically expected Bragg peak positions from the core–shell structure of the NWs in reciprocal space. Further, various effects, which may explain the double structure of the Bragg reflections will be considered. Finally, we will propose a model explaining the origin of the Bragg reflections Peak(1) and Peak(2).

FEM simulations

In order to understand the intensity distribution in reciprocal space of SXRD and AXRD reflections, a 3D model of an InAs$_{0.26}$P$_{0.74}$-InP core–shell NW was developed using the finite element method (FEM). The modeling was performed by commercial software COMSOL Multiphysics 5.4.
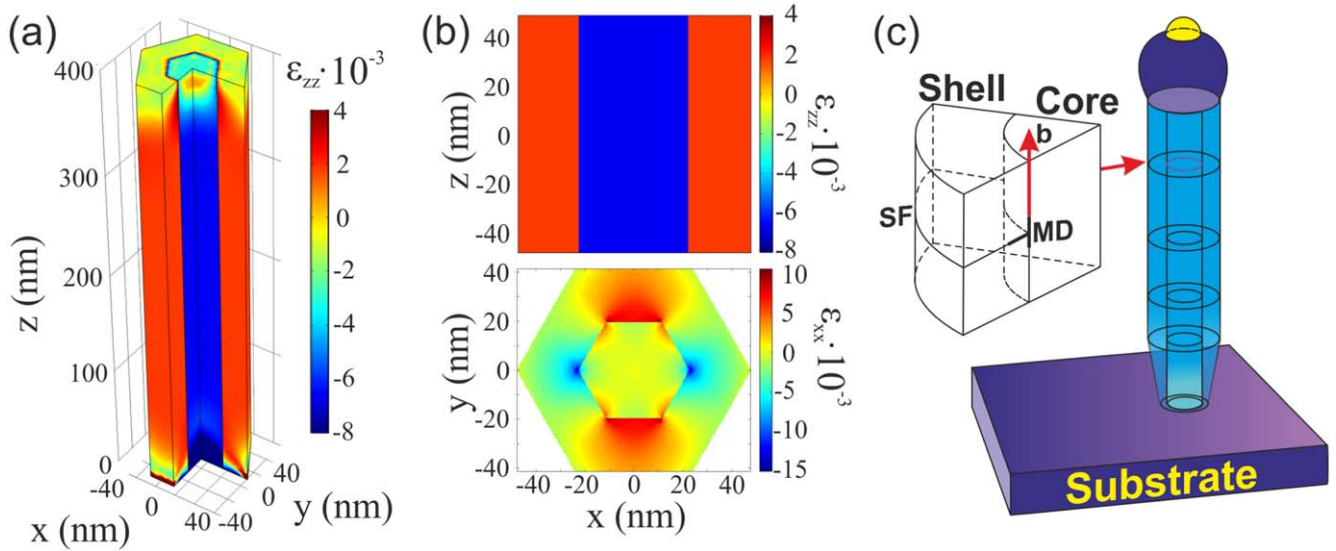
Figure 7. 3D model of a strained core–shell NW with a partial relaxation. (a) The ε_{zz} strain field component of the NW FEM model. The length of the model was chosen to be long enough to avoid the influence of the edge effects in the central part. (b) The strain field components ε_{zz} and ε_{xx} are shown as 2D slices of the model in the xz ($y = 0$) and xy ($z =$ length/2) planes, respectively. (c) Schematic presentation of a model explaining the partial relaxation in InAs$_{0.26}$P$_{0.74}$-InP core–shell NWs due to MDs formation on the core–shell interface. The MDs have circular dislocation lines in the xy-plane with the Burger's vector **b** parallel to z-axis and more probably lead to formation of the stacking faults shown in the model.

Material properties of the shell and core used for the simulations are summarized in the supporting information. According to the Saint-Venant's principle [30], the influence of the ends of the NW on the strain field along its length could be neglected due to the length to diameter ratio of 47.4. Therefore, the length of the FEM model was chosen to be long enough to avoid the influence of the edge effects in the middle of the NW. Further, the values of the central part of the FEM model were used for the modeling.

The strain field component $\varepsilon_{zz}(\mathbf{r}) = \frac{\partial u_z(\mathbf{r})}{\partial z}$ obtained from the FEM model presents the deformation of material along z-direction. Here $u_z(\mathbf{r})$ is the displacement field at each point $\mathbf{r}$ (x, y, z) of the NW. The 3D view of the $\varepsilon_{zz}(\mathbf{r})$ component is shown in figure 7(a). As one can see, the central part is not affected by the strain field variation due to the edges of the model and was set further to the origin of the coordinate of the model. The 2D slices in xz and xy planes of the central part of the model with the strain components ε_{zz} and ε_{xx}, respectively, are shown in figure 7(b). The component $\varepsilon_{xx}(\mathbf{r}) = \frac{\partial u_x(\mathbf{r})}{\partial x}$ is defined through the derivative of the x-component of the displacement field $u_x(\mathbf{r})$ and gives the deformation of the model along x-direction. The strain field component ε_{zz} remains constant in the core and the shell along the NW length, while the ε_{xx} component has complicated spatial distribution.

Further, the average unit cell lattice parameters a and c were obtained from the FEM simulations, which are summarized in tables 1, 2 with the reciprocal space coordinates Q_x, Q_z of the corresponding Bragg reflection. The obtained Q_x, Q_z coordinates represent theoretically expected position of the defect-free InAs$_{0.26}$P$_{0.74}$-InP core–shell NWs Bragg peak in reciprocal space, which is shown in figure 6(b) for the 11$\bar{2}$8

Bragg peak. The tetragonal distortion of the unit cell lattice parameters c and a due to the strain between the core and the shell could be calculated from the FEM model and is $D_{FEM} = -1.2 \pm 0.1 \times 10^{-3}$. This value is different from the D_1 and D_2 calculated above. It can be explained by the fact that the model does not take into account the core–shell relaxation by defects.

Monte Carlo simulation of the diffracted intensity

The strain field in the core–shell NWs obtained from the FEM model and the experimentally obtained, from the WH plot, average tilt of the NWs with respect to the substrate normal were used to simulate the intensity distributions of SXRD and AXRD Bragg reflections of the NWs using the Monte Carlo (MC) method. In the MC simulations, the diffraction pattern of a single NW with the corresponding strain field components ε_{ii} was simulated 10^5 times with the angular distribution obtained from the WH plot. This number of simulations was chosen to be approximately equal to the number of illuminated NWs. The resulting intensity distribution of the 0002 SXRD reflection is presented in figure 4(c) and the 11$\bar{2}$8 AXRD Bragg reflection is shown in figure 6(c). Both RSMs reveal the formation of only one Bragg peak despite the complex strain field components.

It was observed from the TEM and SEM images that the InP shell of the NWs is thinner in the bottom part, closer to the substrate (see the supporting information). This thickness difference may also lead to different relaxation of the core–shell material along the NWs and may lead to additional maxima of intensity in RSMs. In order to investigate the influence of this effect on the scattered x-ray intensity, the shell thickness variation function was obtained from the TEM

measurements, and a model of the NW with InP shell thickness variation was developed. Further, the MC simulated RSMs based on the FEM and this model were compared. It was demonstrated that the effect of the shell thickness variation does not have any significant influence on the scattered x-ray intensity in reciprocal space (see the supporting information).

Discussion

We attribute the most intense diffraction signal Peak(1) registered in our x-ray coplanar diffraction experiments to the scattering from the $InAs_{0.26}P_{0.74}$ WZ core and InP WZ shell adapted to each other along the growth direction of the NWs. This assumption was made based on the fact that the InP shell thickness of the NWs in our experiment was below the critical one for MDs formation. The second less intense diffraction signal Peak(2) is originated most probably from the partially relaxed core due to the relaxation of strain between the core and the shell.

The main effect, which may explain this partial relaxation of the core–shell interface of the NWs and presence of two Bragg peaks, assumes relaxation of the core due to MDs formation between the core–shell interface, which most probably leads to the formation of the stacking faults. In this case, the core is partially relaxed due to the strain field of these defects, and the MDs have the circular dislocation lines in the *xy*-plane on the core–shell interface with the Burgers vectors **b** equal to the unit cell parameter (c_{InAsP}) along the [0001] crystallographic direction [31]. Lattice parameters *a* and *c*, calculated from the FEM model, are smaller than the experimentally obtained from the reflection Peak(1) (see table 2). That might also be due to the strain release by the dislocations between the core and the shell.

The schematic representation of the model explaining the partial relaxation in the NWs due to MDs formation on the core–shell interface is given in figure 7(c). In this case, the linear MD density can be estimated as [32] $\rho \approx (c_{Peak(2)} - c_{Peak(1)})/c^2_{InAsP}$ and is equal to $3.3 \pm 0.3 \times 10^4$ cm^{-1}. Taking into account the low density of MDs and the limited number of recorded HRTEM images, they may be easily missed in our TEM measurements. Moreover, the MDs are located at the core–shell interface and are covered by the shell in the TEM transmission geometry. Therefore, the TEM measurements can not provide information regarding the presence of MDs with the lattice mismatch of only $\sim 5 \times 10^{-3}$, which demonstrates the power of the coplanar x-ray diffraction performed at the synchrotron.

Conclusions

In this work, structural properties of an ensemble of $InAs_xP_{1-x}$-InP core–shell nanowires were investigated employing the coplanar x-ray diffraction geometry. Study of series of symmetric coplanar Bragg reflections allowed us to derive $26\% \pm 3\%$ chemical composition of As in the $InAs_xP_{1-x}$ core. Further, the average tilt of the NWs with respect to the substrate normal was obtained to be $1.68°$ $\pm 0.71°$ using the mosaic model and the Williamson–Hall plot.

Based on the results of x-ray diffraction, scanning and TEM measurements, a model of core–shell relaxation was proposed. The finite element model of the $InAs_xP_{1-x}$-InP core–shell NW helped us to understand the strain field distribution in the NW and the intensity formation in reciprocal space of the asymmetric $11\bar{2}8$ Bragg peaks. Further, we demonstrated that the observed shell thickness variation does not influence the x-ray Bragg peak formation by the Monte Carlo calculations. The second diffraction signal (Peak(2)) observed in the experiment was attributed to the partially relaxed core of the NWs due to a small number of MDs with the circular dislocation lines formed at the core–shell interface. Their linear density was estimated to be $3.3 \pm 0.3 \times 10^4$ cm^{-1}.

Results of our study demonstrate the high sensitivity of the coplanar x-ray diffraction measurements to the MD-induced strain relaxation detection in the NWs and the average structural properties of an ensemble of nanostructures. We hope that this work will contribute to a better understanding of the structure of semiconductor NWs and will help to improve their growth procedure.

ORCID iDs

Sergey Lazarev https://orcid.org/0000-0002-7230-3559
Magnus Borgström https://orcid.org/0000-0001-8061-0746
Maria E Messing https://orcid.org/0000-0003-1834-236X
H Q Xu https://orcid.org/0000-0001-6434-2569
Dmitry Dzhigaev https://orcid.org/0000-0001-8398-9480
Ivan A Vartanyants https://orcid.org/0000-0002-0340-8234

References

[1] Yang P, Yan R and Fardy M 2010 Semiconductor nanowire: what's next? *Nano Lett.* **10** 1529–36
[2] Chen L, Lu W and Lieber C M 2015 *Semiconductor Nanowires: From Next-Generation Electronics to Sustainable Energy* (Cambridge: The Royal Society of Chemistry) pp 1–53
[3] Consonni V and Feuillet G 2014 *Wide Band Gap Semiconductor Nanowires* (New York: Wiley)

[4] Choi H-J 2012 *Semiconductor Nanostructures for Optoelectronic Devices: Processing, Characterization and Applications* ed G-C Yi (Berlin: Springer) pp 1–36

[5] Schroth P *et al* 2015 Evolution of polytypism in GaAs nanowires during growth revealed by time-resolved *in situ* x-ray diffraction *Phys. Rev. Lett.* **114** 055504

[6] Köhl M *et al* 2015 Polytypism in GaAs nanowires: determination of the interplanar spacing of wurtzite GaAs by x-ray diffraction *J. Synchrotron Radiat.* **22** 67–75

[7] Wang N, Tang Y, Zhang Y, Yu D, Lee C, Bello I and Lee S 1998 Transmission electron microscopy evidence of the defect structure in Si nanowires synthesized by laser ablation *Chem. Phys. Lett.* **283** 368–72

[8] Prades J, Arbiol J, Cirera A, Morante J, Avella M, Zanotti L, Comini E, Faglia G and Sberveglieri G 2007 Defect study of SnO₂ nanostructures by cathodoluminescence analysis: application to nanowires *Sensors Actuators* B **126** 6–12 Functional Materials for Micro and Nanosystems

[9] Dzhigaev D, Stankevič T, Besedin I, Lazarev S, Shabalin A, Strikhanov M N, Feidenhans'l R and Vartanyants I A 2015 Theoretical analysis of the strain mapping in a single core–shell nanowire by x-ray Bragg ptychography *Proc. SPIE* **9592** 95920S

[10] Dzhigaev D *et al* 2016 Bragg coherent x-ray diffractive imaging of a single indium phosphide nanowire *J. Opt.* **18** 064007

[11] Dzhigaev D *et al* 2017 X-ray bragg ptychography on a single InGaN/GaN core–shell nanowire *ACS Nano* **11** 6605–11

[12] Lazarev S *et al* 2018 Structural changes in a single GaN nanowire under applied voltage bias *Nano Lett.* **18** 5446–52

[13] Schroth P, Jakob J, Feigl L, Mostafavi Kashani S M, Vogel J, Strempfer J, Keller T F, Pietsch U and Baumbach T 2018 Radial growth of self-catalyzed GaAs nanowires and the evolution of the liquid Ga-droplet studied by time-resolved *in situ* x-ray diffraction *Nano Lett.* **18** 101–8

[14] Magnusson M H, Deppert K, Malm J-O, Bovin J-O and Samuelson L 1999 Size-selected gold nanoparticles by aerosol technology *Nanostruct. Mater.* **12** 45–8

[15] Wallentin J, Messing M E, Trygg E, Samuelson L, Deppert K and Borgström M T 2011 Growth of doped InAsᵧP₁₋ₓ nanowires with InP shells *J. Cryst. Growth* **331** 8–14

[16] Borgström M T, Wallentin J, Trägårdh J, Ramvall P, Ek M, Wallenberg L R, Samuelson L and Deppert K 2010 *In situ* etching for total control over axial and radial nanowire growth *Nano Res.* **3** 264–70

[17] Wallentin J, Jacobsson D, Osterhoff M, Borgström M T and Salditt T 2017 Bending and twisting lattice tilt in strained core–shell nanowires revealed by nanofocused x-ray diffraction *Nano Lett.* **17** 4143–50

[18] Kriegner D, Wintersberger E, Kawaguchi K, Wallentin J, Borgström M T and Stangl J 2011 Unit cell parameters of wurtzite InP nanowires determined by x-ray diffraction *Nanotechnology* **22** 425704

[19] Kriegner D *et al* 2011 Unit cell structure of crystal polytypes in InAs and InSb nanowires *Nano Lett.* **11** 1483–9

[20] Schuster M, Gervais P O, Jobst B, Hösler W, Averbeck R, Riechert H, Iberl A and Stömmer R 1999 Determination of the chemical composition of distorted InGaN/GaN heterostructures from x-ray diffraction data *J. Phys. D: Appl. Phys.* **32** A56–60

[21] Moram M A and Vickers M E 2009 X-ray diffraction of III-nitrides *Rep. Prog. Phys.* **72** 036502

[22] Zhang M and Li X 2017 Structural and electronic properties of wurtzite BₓAl₁₋ₓN from first-principles calculations *Phys. Status Solidi* b **254** 1600749

[23] Boxberg F, Sondergaard N and Xu H Q 2010 Photovoltaics with piezoelectric core–shell nanowires *Nano Lett.* **10** 1108–12

[24] Lazarev S, Bauer S, Forghani K, Barchuk M, Scholz F and Baumbach T 2013 High resolution synchrotron x-ray studies of phase separation phenomena and the scaling law for the threading dislocation densities reduction in high quality AlGaN heterostructure *J. Cryst. Growth* **370** 51–6

[25] Lazarev S, Barchuk M, Bauer S, Forghani K, Holý V, Scholz F and Baumbach T 2013 Study of threading dislocation density reduction in AlGaN epilayers by Monte Carlo simulation of high-resolution reciprocal-space maps of a two-layer system *J. Appl. Crystallogr.* **46** 120–7

[26] Pietsch U, Holy V and Baumbach T 2004 *High-Resolution X-Ray Scattering: From Thin Films to Lateral Nanostructures* (New York: Springer)

[27] Robinson I K 1986 Crystal truncation rods and surface roughness *Phys. Rev.* B **33** 3830–6

[28] Williamson G K and Hall W H 1953 X-ray line broadening from filed aluminium and wolfram *Acta Metall.* **1** 22–31

[29] Mostafavi Kashani S M, Kriegner D, Bahrami D, Vogel J, Davtyan A, Feigl L, Schroth P, Jakob J, Baumbach T and Pietsch U 2019 X-ray diffraction analysis of the angular stability of Self-Catalyzed GaAs nanowires for future applications in solar-light-harvesting and light-emitting devices *ACS Appl. Nano Mater.* **2** 689–99

[30] Toupin R A 1965 Saint-Venant's principle *Arch. Ration. Mech. Anal.* **18** 83–96

[31] Kavanagh K L 2010 Misfit dislocations in nanowire heterostructures *Semicond. Sci. Technol.* **25** 024006

[32] Kaganer V M, Köhler R, Schmidbauer M, Opitz R and Jenichen B 1997 X-ray diffraction peaks due to misfit dislocations in heteroepitaxial structures *Phys. Rev.* B **55** 1793–810